Bulletin of the Seismological Society of America, Vol. 99, No. 2B, pp. 1271–1286, May 2009, doi: 10.1785/0120080153

Study of Rotational Ground Motion in the Near-Field Region

by Marco Stupazzini, Josep de la Puente, Chiara Smerzini, Martin Käser, Heiner Igel, and Alberto Castellani

Abstract During the nineteenth and twentieth centuries observational seismologists recorded primarily the earthquake-induced translational wave field, while the rotational motion still remains poorly observed and investigated. We aim to further understand the rotational ground motion and its relation to the translational wave field, with a special emphasis on the near field, a few wavelengths away from the hypocenter, where damage related to rotational motion might need to be considered. A broad picture of the available values of rotational amplitudes and their variability is obtained by gathering most of the published data on strong rotational motion. To obtain a more detailed picture we perform a large scale 3D numerical study of a strike-slip event in the Grenoble valley where a combination of topographic, source, and site effects produces a realistic wave field. We analyzed the synthetic dataset in terms of the rotational and translational peak amplitudes and their dependence on two effects: nonlinear soil behavior and source directivity. On a soft soil deposit, we observe peak ground rotation of 1 mrad and the peak ground rotation rate of 10 mrad/sec, for an M_w 6.0 event. Those values show a strong dependence on the hypocenter location, the local site conditions, and the topographical features, inducing a variability of almost one order of magnitude in a range of distances of 20 km. Finally, we compare our numerical results in terms of peak ground velocity (PGV) versus peak ground rotation (PGω) with field data obtained at similar scenarios (e.g., Parkfield) by array techniques to investigate the relation between translational and rotational amplitudes expected in the near field for shallow, medium-sized earthquakes. Results of our numerical simulation fit reasonably well with those observed in past studies. Furthermore, the spatial variations of the PGV/PGω ratio show a trend, which is correlated with the velocity structure of the model under study.

Introduction

Earthquakes radiate large amounts of energy, primarily as seismic waves. Studies of the rotational components of ground motion preceded and have lasted longer than both modern seismology (late 1800s to present) and engineering strong-motion seismology (1930s to present; Trifunac, 2009a). Nevertheless, for technical and historical reasons (as clearly explained by Trifunac [2009b]), during the nineteenth century seismologists recorded through different devices (seismometers or accelerometers) only the three degrees of freedom associated with the translational motion (i.e., velocity, $\dot{u} = [\dot{u}_x, \dot{u}_y, \dot{u}_z]$) or acceleration along a Cartesian reference frame, implicitly neglecting the rotational components of the motion. Nevertheless, the investigation of the latter cannot be obviated *a priori* in risk assessment studies, as it has already been acknowledged that rotational ground motion plays a role in the dynamic response and damage induced by certain earthquakes on buildings (Richter, 1958; Newmark, 1969; Stratta and Griswold, 1976; Gupta and Trifunac, 1989; Kalkan and Graizer, 2007).

A direct observation of earthquake-induced rotational ground motion is possible using devices sensitive to torsion such as tilt meters or, more recently, solid-state devices (Nigbor, 1994), ring lasers (Stedman *et al.*, 1995), and broadband rotation meters (Lin *et al.*, 2009). However, such devices are not in common use, and most frequently, the rotational components of motion are indirectly estimated from array measurements (e.g., Spudich *et al.*, 1995; Huang, 2003; Suryanto *et al.*, 2006; Ghayamghamian and Nouri, 2007; Spudich and Fletcher, 2008). The records of translational and rotational components of motion have proved to be useful, for example, in the extraction of local phase velocities, or the back azimuth of events (Igel *et al.*, 2005, 2007), or in recovering the static displacement (Trifunac and Todorovska, 2001; Graizer, 2005, 2006a,b; Pillet and Virieux, 2007). Regardless of the recent interest in the field, studies of recorded rotational ground motion for teleseismic or local events are still rare, and our knowledge of the rotational wave field is largely insufficient.

In spite of the lack of observed data, numerical studies have been performed with the goal of computing synthetic time histories in order to investigate the influence of important factors on rotational motion and, in particular, their expected maximum amplitudes. A pioneering numerical study was accomplished by Bouchon and Aki (1982), and further numerical experiments have followed (Lee and Trifunac, 1987; Takeo, 1998; Wang *et al.*, 2009). In our case, we simulate several events in a 3D model of an Alpine valley at Grenoble, France, with an alluvium-filled basin so that topographic, soil, and source effects can all be considered. The synthetic results are compared with data retrieved mainly from array experiments and investigated in terms of the following ratio, as already done by Fichtner and Igel (2009) and Wang *et al.* (2009):

$$\frac{\mathrm{PGV}_h(\underline{x})}{\mathrm{PG}\omega_z(\underline{x})} \approx 2c_s, \tag{1}$$

where $\mathrm{PGV}_h(\underline{x})$ is the peak ground horizontal velocity value in time computed as $\sqrt{\dot{u}_x^2 + \dot{u}_y^2}$ at location $\underline{x}$, $\mathrm{PG}\omega_z(\underline{x})$ is the peak ground vertical rotation, and c_s can be regarded as a scaling factor between translational and rotational peak ground motion. For a site on parallel layers excited by plane waves, c_s represents the phase velocity of a frequency component (Trifunac, 1982). Furthermore, without any loss of generality the rotational motion can be separated into two parts: one associated with pure shear, involving the contributions from *SH* and Love waves and resulting in rotational motion around the vertical axis (Lee and Trifunac, 1985), and the other one associated with *P*, *SV*, and Rayleigh waves and resulting in rotational motion around the horizontal axis (Lee and Trifunac, 1987). For both decompositions the Fourier spectrum of rotations is proportional to the ratio between the Fourier spectrum of velocity and the phase velocity (Trifunac and Todorovska, 2001).

The separation into two parts implies the knowledge of the polarization of the incident wave field, and this information is not trivial to recover from a practical standpoint, even if some recent work seems to be promising on this issue (Langston *et al.*, 2009).

When the ratio is taken of the peak velocity and peak rotation in time, it becomes an average or equivalent phase velocity at the site. In the absence of recorded strong-motion rotation data, investigating the correlation of this ratio, c_s, with the local velocity allows us to address the question of whether we can obtain reliable peak rotational motion estimates straight from peak ground measurements of translational motions.

This article is structured as follows. First, we give an overview of studies related to rotational ground-motion recordings, both observational and numerical, and the general trends and characteristics observed in them. In the next section, we introduce and validate a 3D method used to simulate the translational and rotational ground motion produced in complex scenarios. A particular case study follows, in which we simulate an M_w 6.0 strike-slip earthquake occurring in the Grenoble valley. Moreover, we compare the rotational wave field at both the bedrock and the sedimentary basin, and we draw peak ground motion maps for different magnitudes, sediment mechanical properties, and source hypocenter locations. Finally, we put our synthetic dataset in direct comparison with past simulations and observations in terms of the ratio given by equation (1) to draw conclusions about the correlation between translational and rotational ground motion and its physical implications.

Past Studies in Rotational Seismology

In the past decades few studies have shown direct measurements of rotations, thus leading to large uncertainties in the order of magnitude of rotations likely to occur for a given earthquake scenario. Therefore, it is important to synthesize in a comprehensive way a selection of the data available in the literature. Specifically, we chose data that might be of relevance for seismic engineering studies, namely, those recorded in the near field (a few wavelengths away from the epicenter) or showing relatively strong rotation amplitudes, even if recorded at greater distance.

For the sake of completeness, we combine field data records with synthetic studies, observations at stiff and soft soils, array-derived with single-point measurements and those generated by different source mechanisms. Proper labeling helps to subdivide them into groups that can be directly compared to each other. In the following, we briefly present the sources of data that we use and that are listed in Table 1.

A pioneering work was published by Bouchon and Aki (1982), who adopted a semianalytical method to derive strains, tilts, and rotations in the proximity of a buried 30 km long strike-slip fault with seismic moment 8×10^{18} N m, obtaining a peak ground rotation on the order of 3×10^{-4} rad while the corresponding rotational rate was about 1.5×10^{-3} rad/sec. Following this work, different analyses have tried to record and characterize ground rotational motions. Most of these studies are based on indirect estimates of surface ground rotations from 2D seismic arrays (see Castellani and Boffi, 1986; Oliveira and Bolt, 1989; Bodin *et al.*, 1997; Singh *et al.*, 1997; Huang, 2003; Spudich and Fletcher, 2008). The most significant drawback of such an approach is the limited frequency content (typically lower than 2 Hz) due to the relatively large separation distance between adjacent receivers. Besides field observations, ground rotations have also been investigated from a theoretical point of view. Those studies rely either on the theory of elastodynamics for plane wave propagation in ideal media (Trifunac, 1982; Lee and Trifunac, 1985) or on kinematic source models (Takeo and Ito, 1997). The direct measurement of rotations has been obtained at great distances from important earthquakes using ring laser instruments (McLeod *et al.*, 1998; Pancha *et al.*,

Table 1

List of Selected Literature Data

Reference	Number	Data Type*	Earthquake Parameters			Type of Soil‡	PGV_h (m/sec)	$PG\omega_z$ (rad)	$PG\dot{\omega}_z$ (rad/sec)	Symbol
			M_w	R (km)	Source Mechanism†					
Bouchon and Aki (1982)	1	2	6.6	1	SS	1	1	2×10^{-4}	1.2×10^{-3}	▼
	2		6.6	1	SS	1	1.6	3×10^{-4}	1.5×10^{-3}	▼
Lee and Trifunac (1985)	3	2	6.6	10	N.A.	1	0.45	1×10^{-4}	1.2×10^{-3}	▼
Niazi (1986)	4	1	6.6	5	SS	2	0.203	2.75×10^{-4}	7×10^{-4}	△
Oliveira and Bolt (1989)	5	1	5.6	6	N.A.	1	0.15	7.4×10^{-6}	N.A.	▲
	6		5.7	30	N.A.	1	0.12	8.5×10^{-6}	N.A.	▲
	7		5.8	22	N.A.	1	0.30	1.46×10^{-5}	N.A.	▲
	8		6.7	84	N.A.	1	0.06	6.8×10^{-6}	N.A.	▲
	9		7.8	79	N.A.	1	0.391	3.93×10^{-5}	N.A.	▲
Castellani and Boffi (1986)	10	2	6.6	18	SS	1	0.0692[3]	3.06×10^{-5}	1.04×10^{-4}	▼
Nigbor (1994)	11	3	1 kton	1	Expl.	1	0.2780	6.6×10^{-4}	2.4×10^{-2}	×
Bodin *et al.* (1997); Singh *et al.* (1997)	12	1	6.7	311	R	2	0.03	5.6×10^{-5}	N.A.	△
	13		7.5	305	R	2	0.11	2.07×10^{-4}	N.A.	△
Takeo (1998)	14	3	5.7	3.3	SS	1	0.29	N.A.	3.3×10^{-3}	×
	15	3	5.3	3.3	SS	1	0.20	N.A.	8.1×10^{-3}	×
Huang (2003)	16	1	7.7	6	T	1	0.33	1.71×10^{-4}	N.A.	▲
Data retrieved with the methodology illustrated in Paolucci and Smerzini (2008).	17	1	4.2	81	N.A.	2	4.06×10^{-4}	Mean 1.64×10^{-7} min 8.79×10^{-8} max 3.38×10^{-7}	2.4×10^{-4} 1.75×10^{-4} 4.7×10^{-4}	◯ with vertical bar
	18		4.9	81	N.A.	2	5.2×10^{-3}	Mean 2.25×10^{-6} min 1.16×10^{-6} max 3.33×10^{-6}	3.2×10^{-3} 1.8×10^{-3} 5.0×10^{-3}	◯ with vertical bar
	19	1	6.0	11.6	SS	1	0.25	Mean 8.98×10^{-5} min 4.07×10^{-5} max 1.51×10^{-4}	1.3×10^{-3} 3.5×10^{-4} 1.6×10^{-3}	● with vertical bar
	20		6.5	65	SS	1	0.165	Mean 7.68×10^{-5} min 4.23×10^{-5} max 1.25×10^{-4}	8.2×10^{-4} 2.8×10^{-4} 1.6×10^{-3}	● with vertical bar
Spudich and Fletcher (2008)	21	1	6.0	8.8	SS	1	0.25 0.20 0.28 0.27	Broad Band 8.81×10^{-5} Array 1–3 $2.25E-05$ Array 8–11 $6.17E-05$ Array 5–12 $3.56E-05$	1.09×10^{-3} 1.39×10^{-4} 4.48×10^{-4} 2.23×10^{-4}	△
	22		4.7	14.0	SS	1	1.19×10^{-2} 1.27×10^{-2} 9.16×10^{-2} 1.19×10^{-2}	Broad Band 4.69×10^{-6} Array 1–3 1.64×10^{-6} Array 8–11 1.88×10^{-6} Array 5–12 1.43×10^{-6}	9.44×10^{-5} 9.12×10^{-6} 1.08×10^{-5} 7.47×10^{-6}	small dark gray triangle

(*continued*)

Table 1 (*Continued*)

Reference	Number	Data Type*	Earthquake Parameters			Type of Soil‡	PGV_h(m/sec)	$PG\omega_z$ (rad)	$PG\dot{\omega}_z$ (rad/sec)	Symbol
			M_w	R (km)	Source Mechanism†					
	23		5.1	14.4	SS	1	6.0210^{-2}	Broad Band 2.0×10^{-5}	4.46×10^{-4}	small light gray triangle
							4.41×10^{-2}	Array 1–3 3.48×10^{-6}	2.10×10^{-5}	
							5.96×10^{-2}	Array 8–11 5.14×10^{-6}	3.22×10^{-5}	
							6.91×10^{-2}	Array 5–12 4.42×10^{-6}	2.49×10^{-5}	
	24		4.9	18.3	SS	1	2.74×10^{-2}	Broad Band 1.36×10^{-5}	2.47×10^{-4}	small black triangle
							2.0×10^{-2}	Array 1–3 2.73×10^{-6}	1.23×10^{-5}	
							3.0×10^{-2}	Array 8–11 5.67×10^{-6}	2.69×10^{-5}	
							3.15×10^{-2}	Array 5–12 3.16×10^{-6}	1.64×10^{-5}	

The data are mainly recorded in the near field (a few wavelengths away from the epicenter) or show relatively strong rotation amplitudes even if recorded at a greater distance. The following quantities are shown: peak values of horizontal ground velocity (PGV_h), vertical ground rotation ($PG\omega_z$), and rotational velocity ($PG\dot{\omega}_z$) about the vertical axis. Additional information regarding the data type, the source parameters (magnitude, epicentral distance R, and source mechanism), and type of soil (a simplified classification was assumed between soft and stiff soil) is included.

*1 indicates array-derived data (▲ or ● with a vertical bar indicate data from numbers 17 to 20). 2 indicates numerical/semianalytical data (▼). 3 indicates measured data (×).

†SS indicates strike slip, T indicates thrust, and R indicates reverse.

‡The distinction between soft and stiff soil was based on V_{S30}. The soil is considered soft if $V_{S30} < 300$ m/sec. In this column, 1 indicates stiff soil (solid symbols, e.g., ▲ or ● with vertical bar) and 2 indicates soft soil (open symbols, e.g., △ or ◯ with vertical bar).

2000; Igel *et al.*, 2005; Cochard *et al.*, 2006; Igel *et al.*, 2007) and in the near field through triaxial rotational sensors (Nigbor, 1994; Takeo, 1998). In particular, Nigbor measured an explosive source, whereas Takeo recorded an earthquake swarm in 1997, offshore the city of Ito in Japan. The two largest events of that swarm have seismic moments of 1.2×10^{17} N m and 2.7×10^{16} N m and were recorded 3.3 km from the fault. The maximum measured rotational rates around the vertical axis were 3.3×10^{-3} rad/sec and 8.1×10^{-3} rad/sec, respectively, several times higher than what was predicted by Bouchon and Aki (1982), even though the seismic moment of the two events was about two orders of magnitude smaller than the one simulated by the authors. This discrepancy cannot be explained as a malfunction or limited sensitivity of the instruments; therefore, the author claimed that the large rotational velocities might be induced by either the heterogeneity of slip velocity along the fault or the local rheology. These two factors may play a crucial role, particularly in the near field, as was stressed by Huang (2003) and Spudich and Fletcher (2008).

Numerical Method Validation

As a complement to the recorded data, we use synthetic rotational seismograms obtained with the spectral element method (SEM), first introduced for the solution of the elastodynamic problems by Priolo et al. (1994), Faccioli *et al.* (1997), and Komatitsch and Vilotte (1998). Here, we adopt the version implemented in the software package GeoELSE (Stupazzini *et al.*, 2009). In order to validate the reliability of the rotational output produced by our method, we compare our results with those obtained with the highly accurate arbitrary high-order derivatives discontinuous Galerkin (ADER-DG) method (Dumbser and Käser, 2006; Käser and Dumbser, 2006).

Both numerical codes have been used on the Höchstleistungsrechner in Bayern (HLRB) 2 of the Leibniz Rechenzentrum München and on the tectonic high performance simulator (TETHYS) cluster (Oeser *et al.*, 2006) of the Department of Earth Sciences and Geophysics at Ludwig-Maximilians-Universität München.

Both methods are essentially high-order finite element methods explicit in the time domain, able to accurately model large velocity contrasts, attenuation effects, and finite-source kinematics, all of which are crucial aspects for reproducing realistic earthquake scenarios in complex geological configurations. In the SEM-based code, absorbing boundaries are implemented through the Stacey (1988) first-order P3 paraxial conditions.

We first choose to cross-validate the synthetics produced by our methods, both translational and rotational, for two established tests proposed by the Southern California Earthquake Center (Day *et al.*, 2007). These are the so-called layer over half-space (LOH) LOH.1 and LOH.2 tests. Both of them describe a flat half-space on top of which lies a thin low-velocity layer. The main difference between both tests is that LOH.1 uses a point source whereas LOH.2 uses a source with a finite extent, thus leading to different waveforms and frequency contents. For the translational motion both methods have already been tested against quasi-analytical solutions (Stupazzini, 2004, Dumbser and Käser, 2006). The setup of the tests and an example of the computational mesh for SEM are depicted in Figure 1. The parameters describing both models are shown in the legend. Besides the translational motion ($\underline{u} = [u_x, u_y, u_z]$), we output rotational ground motion, which is defined as

$$\omega_x = \frac{1}{2}\left(\frac{\partial u_z}{\partial y} - \frac{\partial u_y}{\partial z}\right), \qquad \omega_y = \frac{1}{2}\left(\frac{\partial u_x}{\partial z} - \frac{\partial u_z}{\partial x}\right), \qquad \omega_z = \frac{1}{2}\left(\frac{\partial u_y}{\partial x} - \frac{\partial u_x}{\partial y}\right), \tag{2}$$

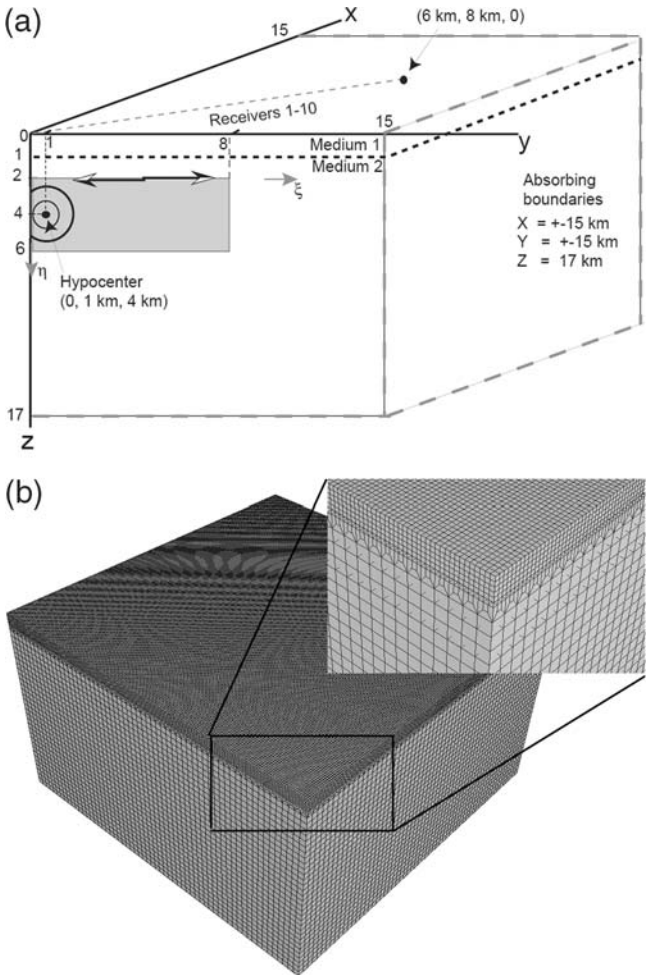

Figure 1. (a) One of four symmetric quarters of the LOH (Day *et al.*, 2001) test cases, consisting of a surface layer 1 km thick (material 1: $\rho = 2600$ kg/m^3, $V_S = 2000$ m/sec, $V_P = 4000$ m/sec) overlying bedrock (material 2: $\rho = 2700$ kg/m^3, $V_S = 3464$ m/sec, $V_P = 6000$ m/sec). The hypocenter and rupture surface of case LOH.2 are also shown, together with the receiver locations for Figure 2. (b) Spectral element mesh adopted for the LOH.1 and LOH.2 cases. Notice the mesh refinement at the low-velocity layer.

and the corresponding rotational velocities and accelerations

$$\dot{\omega}_i = \frac{d\omega_i}{dt}, \qquad \ddot{\omega}_i = \frac{d^2\omega_i}{dt^2} \quad \text{with } i = x, y, z. \tag{3}$$

A comparison of the synthetics obtained with both methods can be found in Figure 2. In this case, the SEM solution has been computed with a mesh of 352,800 hexahedral elements using polynomials of degree four to describe the variables, while the ADER-DG solution has been computed with polynomials of degree three and a mesh with 782,542 tetrahedral elements. The agreement between both methods is remarkable, and after only 7 sec some major differences arise owing to the spurious reflections coming from the absorbing boundaries. It can be further observed that the ω_z motion is delayed with respect to other signals, as it is sensitive only to *SH* motion. Similar results characterized the records of all stations.

From these tests we conclude that both methods' solutions are in satisfactory agreement, and that they are able to produce reliable translational and rotational synthetic seismograms in 3D setups.

A Study Case: Grenoble Valley (French Alps)

Studies by Bouchon and Aki (1982), Lee and Trifunac (1985), and Castellani and Boffi (1986) indicated that rotational ground motion could be important in the near field and for surface waves. Although in recent times direct (Nigbor, 1994; Takeo, 1998) and indirect (Graizer, 1989; Huang, 2003) measurements of rotation have received a certain emphasis, the number of available records is still extremely limited; furthermore, there are only a few examples of data in the near-field region (Spudich and Fletcher, 2008). As a consequence our level of knowledge on the magnitude of rotational ground motions to be expected for a given earthquake scenario is still limited.

In this article we make use of 3D numerical modeling to reproduce the rotational wave field generated by strike-slip earthquakes in the near field. We choose as our study area the Grenoble valley (French Alps) for two main reasons. First, when it comes to large scale numerical simulations the validity of the results is hard to assess. As models grow complex the amount of parameters to be taken into account increases severely, as does the possibility of introducing unexpected errors in the computation. The Grenoble case, in particular, has the great advantage of having been successfully bench-

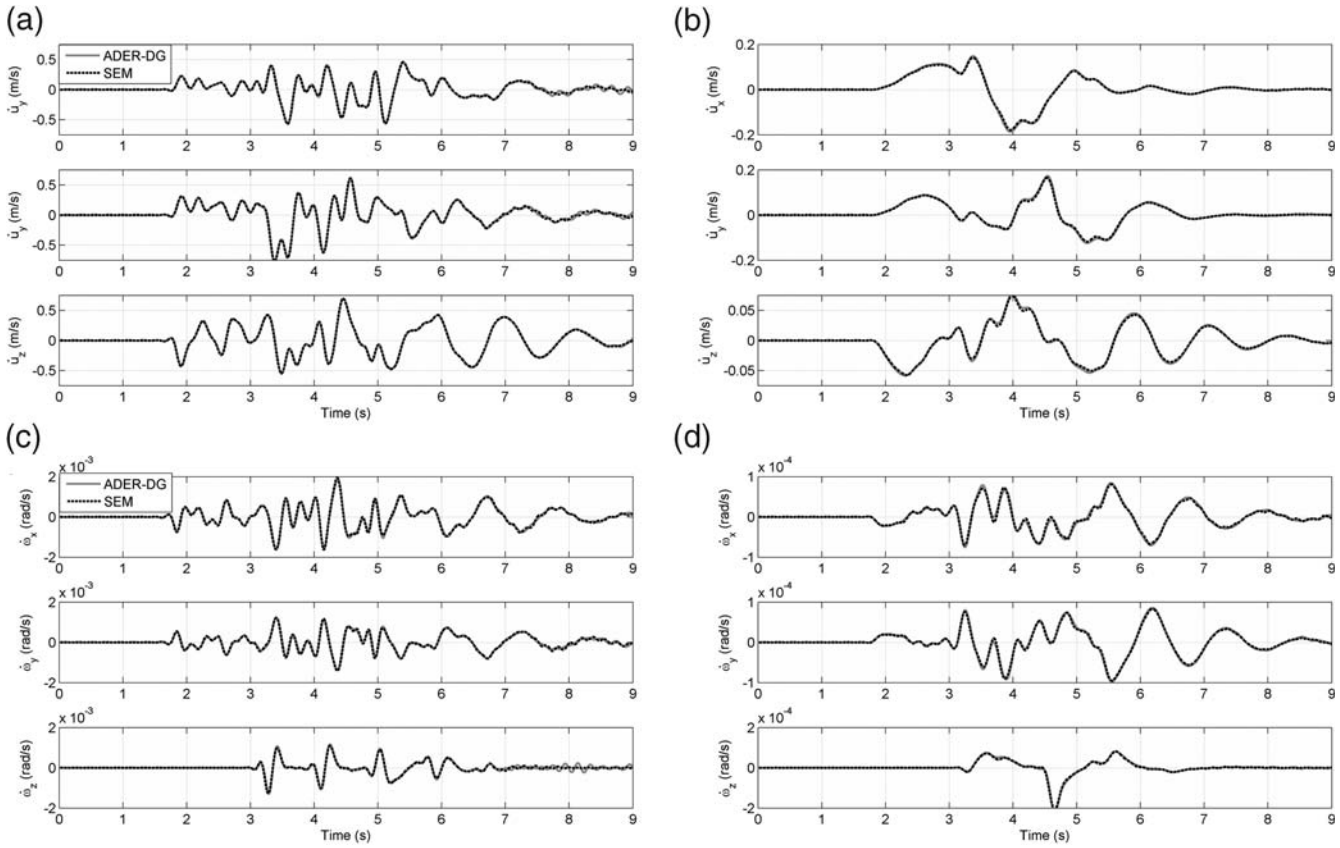

Figure 2. Comparison of the translational (a) and (b) and rotational rates (c) and (d) for the LOH.1 (a) and (c) and LOH.2 (b) and (d) test cases at the surface. The receiver coordinates are (6000, 8000, 0) m. The SEM solution is plotted in black, and the ADER-DG solution is plotted in gray.

marked by cross-validation between many state-of-the-art simulation techniques (Chaljub, 2006) including the SEM and ADER-DG methods used in the previous section. This significantly increases our degree of confidence in the synthetic results. A second but not less important reason is the fact that the Grenoble valley offers the chance to investigate many factors, which can be crucial for amplification phenomena in the near field such as site, topographic, and source directivity effects.

The model of the Grenoble valley has been constructed using a 250 m resolution digital elevation model (DEM) of the surrounding topography and of the shape of the basin. The basin's soil is described by the following polynomial variation with depth z (measured in meters):

$$V_P = 1450 + 1.5z, \qquad V_S = 300 + 19z^{1/2}, \qquad \rho = 2140 + 0.125z, \qquad Q_S = Q_P = 50, \tag{4}$$

where V_P and V_S are the P- and S-wave velocities (in m/sec), respectively, ρ is the mass density (in kg/m^3), and Q_P and Q_S are P- and S-wave quality factors. The surrounding bedrock is two-layered, with $V_P = 5600$ m/sec and $V_S = 3200$ m/sec between 0 and 3 km depth and $V_P = 5920$ m/sec and $V_S = 3430$ m/sec between 3 and 27 km depth.

In the following, the GeoELSE version of the SEM has been used to compute the synthetic seismograms. A linear viscoelastic material is used to model the attenuation. The final computational mesh consists of 216,972 elements, the size of which ranges from a minimum of about 20 m inside the alluvial basin up to 900 m at some bedrock areas. The mesh has been designed to propagate frequencies up to 2 Hz. A detailed description of the mesh generation can be found in Stupazzini *et al.* (2009).

We use the source specification denoted as the strong motion 1 case by Chaljub (2006), which corresponds to an M_w 6.0 earthquake originated at the eastern segment of the Belledonne Border fault (see Fig. 3a). The fault is defined as a 9 $\times$ 4.5 km rectangle where inplane rupture occurs with a uniform slip of 1 m. The mechanism is strike-slip right-lateral (strike equals 45°, dip equals 90°, and rake equals 180°). The rupture propagates circularly from the hypocenter located at the center of the fault with velocity v_r = 2.8 km/sec. The time history of the seismic moment tensor source is described by an approximate Heaviside function of the type

$$M_0(t) = \frac{1}{2}\left[1 + \mathrm{erf}\left(2.0\frac{t-2\tau}{\tau/2}\right)\right], \tag{5}$$

where erf is the error function and $\tau = 1.116$ sec is a rise time. These values are selected for the slip velocity to be approximately 1 m/sec. A total of 750 spectral nodes are contained in the fault. In the following sections, we also refer to a smaller earthquake (M_w 4.5) simulated for the same fault plane. In that case, we use a smaller rectangular fault, measuring 4 $\times$ 3 km, where the total slip has been reduced to a value of 0.02 m, leaving the remaining parameters unchanged with respect to the M_w 6.0 event.

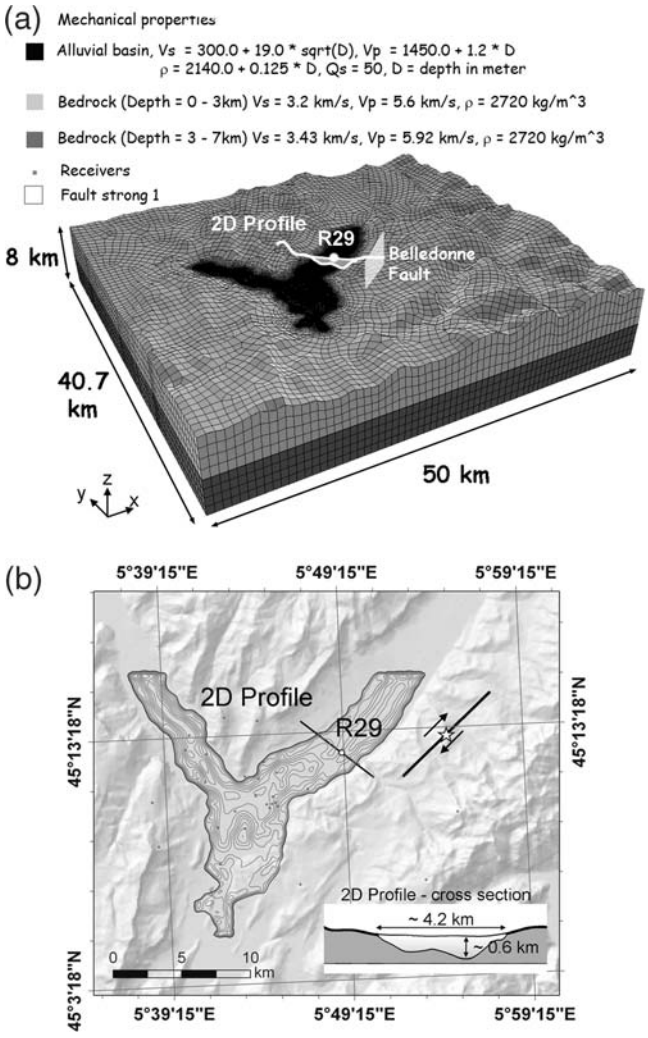

Figure 3. (a) The 3D hexahedral spectral element mesh used for the computation of the Grenoble scenario with the GeoELSE software package. For simplicity, the spectral elements are shown without the Gauss-Lobatto-Legendre nodes. (b) Topography and alluvial basin shape.

Figure 4 presents synthetic velocity and rotational waveforms recorded on a receiver located in the middle of the 2D profile (Fig. 3), namely, R29 of the Grenoble benchmark specification (Chaljub *et al.*, 2007; Dumbser *et al.*, 2007), obtained with the source denoted as strong motion 1. Figure 5 compares velocity and the scaled torsion amplitude spectra of R29 (scaling factor is equal to 2000). Referring to Trifunac (1982) and Spudich and Fletcher (2008), this figure shows that ground torsion spectra are related to the velocity spectra through a suitable scaling factor. The issue regarding the correlation of the latter with the actual equivalent propagation

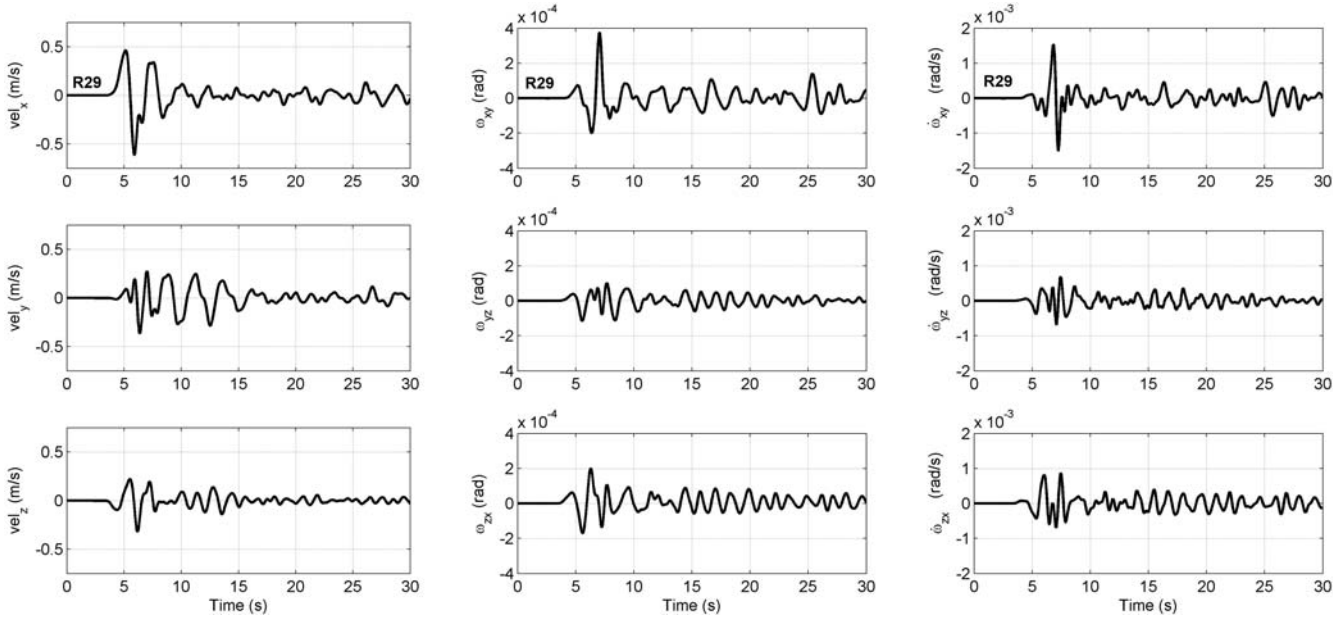

Figure 4. Synthetic velocity and rotational waveforms recorded on a receiver located in the middle of the 2D profile (Fig. 3), namely, R29 of Grenoble benchmark specification (Chaljub *et al.*, 2007; Dumbser *et al.*, 2007), obtained with source denoted as strong motion 1 and by SEM.

velocity, the velocity structure of the basin, and local site conditions will be addressed in the section Synthetic Ratios between Translational and Rotational Peak Values.

Parametric Study of Near-Fault Earthquake Ground Motion in the Grenoble Valley

Our study of the Grenoble M_w 6.0 scenario begins by investigating the effect of various parameters in the rotational and translational motion records. This allows us to discern which parameters more strongly affect the rotational wave field and to get a wider view on the variability of the amplitudes that we can expect. In particular, we record the peak ground motion recorded at a very dense array of synthetic stations inside and near the alluvial basin of Grenoble. Our observables are the peak ground vertical rotation, PGω_z, and the peak ground horizontal rotation, PGω_h, defined as the maximum of $|\omega_z|$ and of $\sqrt{\omega_x^2 + \omega_y^2}$, respectively. Similarly, we use the peak of their respective time derivatives or rates (PG$\dot{\omega}_z$ and PG$\dot{\omega}_h$).

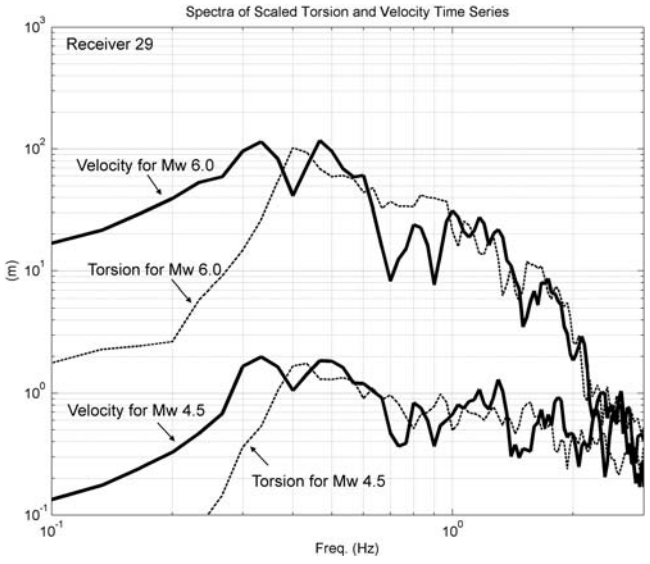

Figure 5. Velocity (black thick lines) and scaled torsion (thin dashed lines) amplitude spectra of R29 for M_w 6.0 and 4.5.

In this contribution, two main phenomena are studied: source directivity and the presence of a nonlinearly behaving soil at the basin. The source directivity effect for the Grenoble case was studied by Stupazzini *et al.* (2009) and has been recomputed here, now outputting the rotational motion components. Three different directivity cases are studied: neutral, forward, and backward. In the neutral case, the hypocenter is located in the middle of the fault plane (hypocenter 1), as described in last section. The other two cases consider that the hypocenter is situated very close to the northeast or southwest tips of the fault (hypocenters 2 and 3, respectively), while keeping the total slip and the slip rate function unaltered. As a result, all three earthquakes have the same magnitude, but their radiation pattern is much larger in the direction directly opposed to their hypocenter position. The exact location of the hypocenters for all three cases can be seen in Figure 6.

The second source of variability of ground motion is the presence of a nonlinear viscoelastic (NLE) soil, instead of the linear viscoelastic (EL) one. The NLE soil model implemen-

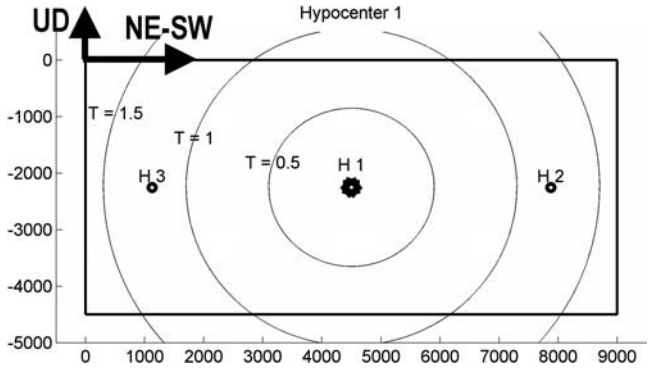

Figure 6. Hypocenter location possibilities. Isochrones of the triggered slip starting from hypocenter 1 are shown as thin lines. The rupture propagates circularly from the selected hypocenter with $v_r = 2800$ m/sec.

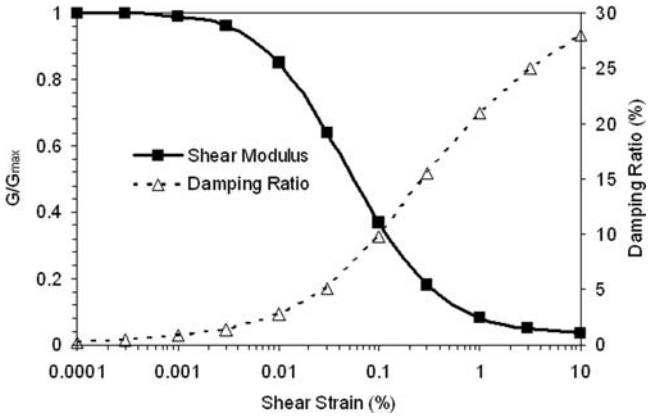

Figure 7. Curves of normalized shear modulus (G) and damping ratio (D) as a function of shear strain (γ), adopted for the alluvium shallow materials in the Grenoble basin (Jerram *et al.*, 2006).

ted in GeoELSE can be regarded as a generalization to 3D load conditions of the classical G-γ and D-γ curves used within 1D linear equivalent approaches (e.g., Kramer, 1996), where G, D, and γ are shear modulus, damping ratio, and 1D shear strain, respectively. Namely, to extend those curves to the 3D case, a scalar measure of shear-strain amplitude was considered as

$$\gamma_{\max}(\underline{x}, t) = \max[|\varepsilon_{\mathrm{I}}(\underline{x}, t) - \varepsilon_{\mathrm{II}}(\underline{x}, t)|, |\varepsilon_{\mathrm{I}}(\underline{x}, t) - \varepsilon_{\mathrm{III}}(\underline{x}, t)|, |\varepsilon_{\mathrm{II}}(\underline{x}, t) - \varepsilon_{\mathrm{III}}(\underline{x}, t)|], \quad (6)$$

where ε_{I}, $\varepsilon_{\mathrm{II}}$, and $\varepsilon_{\mathrm{III}}$ are the principal values of the strain tensor. Once the value of $\gamma_{\max}$ is calculated at the generic position $\underline{x}$ and generic time t, this value is introduced in the G-γ and D-γ curves, and the corresponding parameters are updated for the following timestep. Therefore, unlike the classical linear equivalent approach, the initial values of the dynamic soil properties are recovered at the end of the excitation. The G-γ and D-γ curves specifically calibrated on the Grenoble shallow soil materials described by Jerram *et al.* (2006) were adopted in this work (Fig. 7).

The results of our parametric study have been partly plotted in Figure 8. The first column shows the peak ground rotational motion with the assumption of EL material inside the alluvial basin, while the second column shows analogous results with NLE material. The three rows present the different results obtained with backward (Hypo3), neutral (Hypo1), and forward (Hypo2) directivity. Finally, the combined effect of directivity and linear–nonlinear soil descriptions is summarized in Table 2 in terms of PGω and PG$\dot{\omega}$. The results here are provided for the entire parametric study and the various subareas in which the Grenoble valley was subdivided (Fig. 9).

As a reference, we can take the values obtained for an EL basin with neutral directivity. In this case, we observe peak values of PG$\omega_z = 1.69$ mrad and PG$\omega_h = 1.31$ mrad for the rotations and PG$\dot{\omega}_z = 8.24$ mrad/sec and PG$\dot{\omega}_h = 8.66$ mrad/sec for the rotation rates, primarily recorded at the southern tip of the Y-shaped basin (area 2 of Table 2 and Fig. 9) owing to the constructive interference between the local sedimentary structure and the radiation pattern. As a general trend (see Table 2) we can observe that the combination of forward directivity and nonlinear elasticity produces the strongest rotational motions, whereas the combination of backward directivity and linear elasticity produces the smallest amplitudes.

Another conclusion from our study is that, for the earthquake source used in this example, two main potentially dangerous areas can be identified. One of them is the whole southern tip (area 2 of Table 2 and Fig. 9) of the basin, and the other is the part of the basin located closest to the fault, its northeastern tip (area 1 of Table 2). Peak rotation and rotation rate maxima are consistently recorded at those two areas, particularly at their easternmost sides. This clustering of the maxima toward the edge of the basin is further increased in the presence of nonlinear soils (see Fig. 8). On the other hand, the northwestern tip of the basin (area 3 of Table 2) always records values of rotation and rotation rates around five times smaller than the other basin areas.

The observed range of variability from worst to best case for both rotation and rotation rate maxima is around a factor of 3 for the vertical components and around a factor 6 for the horizontal components. Most of the variation is coming from directivity effects, although the nonlinear soil behavior can also play a significant role (see Table 2). Previous fault normal PGV studies (Stupazzini *et al.*, 2009) found a similarly strong effect of the directivity on the maximum recorded PGV values, which can range from 0.35 m/sec for an H_3 seismic source up to 2.09 m/sec for an H_2 seismic source. As a consequence, both 3D and soil effects produce large spatial variability in the rotational motion, which cannot be accounted for using simplified models (i.e., 2D models or only viscoelastic constitutive behavior).

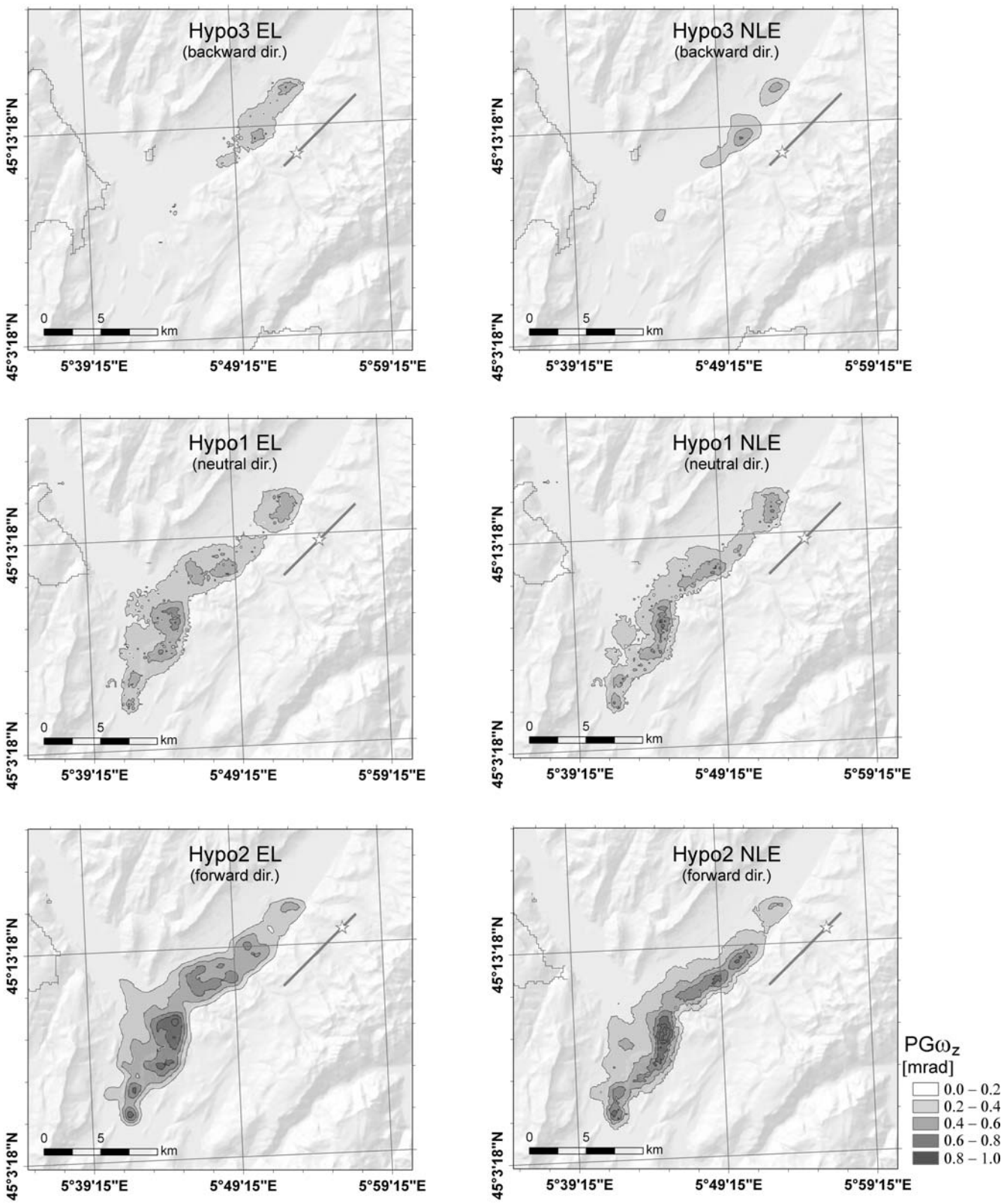

Figure 8. Set of 3D simulations used as parameter study. Maps of PGω_z. Six scenarios are considered: backward directivity (hypocenter 3), neutral directivity (hypocenter 1), and forward directivity (hypocenter 2) characterized by EL and NLE soil behavior.

Table 2

Maximum PGω (mrad) and PG$\dot{\omega}$ (mrad/sec) Motion for Hypocenters Considered in This Parametric Study

	Area 1				Area 2				Area 3				Bedrock	
Hypocenters	EL	NLE	EL	NLE	EL	NLE	EL	NLE	EL	NLE	EL	NLE	EL	EL
	PGω_z		PGω_h		PGω_z		PGω_h		PGω_z		PGω_h		PGω_z	PGω_h
1	1.15	1.22	0.74	0.91	1.69	1.54	1.31	1.75	0.44	0.48	0.52	0.55	0.15	0.16
2	1.74	1.80	1.48	1.98	1.56	2.20	1.89	3.15	0.38	0.40	0.44	0.45	0.28	0.09
3	0.94	1.34	0.63	0.70	0.44	0.48	0.26	0.30	0.33	0.38	0.34	0.35	0.17	0.11
	PG$\dot{\omega}_z$		PG$\dot{\omega}_h$		PG$\dot{\omega}_z$		PG$\dot{\omega}_h$		PG$\dot{\omega}_z$		PG$\dot{\omega}_h$		PG$\dot{\omega}_z$	PG$\dot{\omega}_h$
1	5.33	8.08	4.10	6.38	8.24	9.53	8.66	13.90	1.85	2.37	2.19	2.13	0.71	0.52
2	7.34	12.73	8.01	13.49	8.84	15.54	12.62	25.49	1.40	2.10	1.71	1.90	1.35	0.51
3	5.43	9.86	3.94	5.33	2.08	2.72	1.84	2.17	1.38	1.47	1.52	1.51	0.88	0.64

Results are subdivided into four areas: three located on soft sediments (1, 2, and 3) and the surrounding bedrock as illustrated in the sketch (Fig. 9). The abbreviations EL and NLE refer to the viscoelastic and nonlinear viscoelastic analyses, respectively.

Synthetic Ratios between Translational and Rotational Peak Values

In this section we explore the extent to which rotational and translational motions are correlated; in particular, we address the question of whether we can have a reasonable estimate of peak rotational motion from the corresponding translational motion studies in near-source regions. In this contribution we rely on simplified models (see, e.g., Igel *et al.* [2005, 2007] and Cochard *et al.* [2006]), which assume an incident transversally polarized plane wave, for example, along the y axis. This implies that the displacement can be described as $\underline{u} = [0, u_y(t - x/V_a), 0]$, where V_a is the phase velocity. Under this assumption, at any time, transverse acceleration and rotation rate (or equivalently, velocity and rotation) are in phase, and the amplitudes are related by

$$\dot{u}_y(\underline{x}, t)/\omega_z(\underline{x}, t) = -2V_a. \tag{7}$$

The assumption of plane-wave incidence is expected to hold for a considerable part of the observed ground motion whenever the epicentral distance is large compared to the considered wavelengths and source dimensions (Igel *et al.*, 2005). In the near-field region the hypothesis of plane wave is no longer valid, and a larger variability of the ratio can be expected.

Nevertheless, Wang *et al.* (2009) showed that the ratio between peak ground acceleration (PGA) and rotation rate

Figure 9. Illustration of the subdivision of the results of the parametric study for the different hypocenters considered. Areas 1, 2, and 3 are located on soft sediments. The surrounding area is bedrock (see Table 2).

(PGA$_h(\underline{x})$/PG$\dot{\omega}_z(\underline{x}) = 2c_s$), equivalent to rotation (equation 1), could provide important information regarding the basin structure even in the near field. Wang *et al.* (2009) analyzed a hypothetical M_w 7.0 strike-slip event occurring along the Newport–Inglewood fault embedded in the 3D Los Angeles basin and showed that high values of c_s are located outside the basin and low values are located inside. The only exception to the proportionality between translational and rotational motion happens in the region around the fault, where the c_s value could be used to constrain the rupture process (Takeo and Ito, 1997; Takeo, 1998). In the following we present maps of the ratio between peak ground velocity and rotation.

The quantity c_s in equation (1) is the scaling factor between translational and rotational peak ground motions as estimated by either empirical or numerical data. Under the assumption that *SH* and Love waves are the predominant contributions, which seems a reasonable approximation in the proximity of shallow strike-slip events (as in the Grenoble case), equation (1) provides a simplified approach for evaluating V_a.

Applying equation (1) to the set of 14,400 six-component synthetic seismograms at the Grenoble basin and surrounding area, we obtain the map of the value of c_s at the model's surface. The results regarding the northern part of the model are plotted in Figure 10b, where we can see how the basin (black area) is clearly distinguishable from the surrounding bedrock. We recall that the basin has *S*-wave velocities varying with depth according to equation (4), whereas the bedrock is a homogeneous material with 3200 m/sec *S*-wave velocity, and we recall that the two northern tips of the Y-shaped alluvial basin of Grenoble end abruptly according to the benchmark specification. In addition, we observe a strong correlation between c_s and the depth basin map (Fig. 3b). Furthermore, we aim at investigating the effect that has the pronounced topography (Fig. 10a) in the surrounding area of the Grenoble valley on the rotational and translational wave field. Figure 10c and b shows the PGV$_h$ and PGω_z maps, respectively, with an

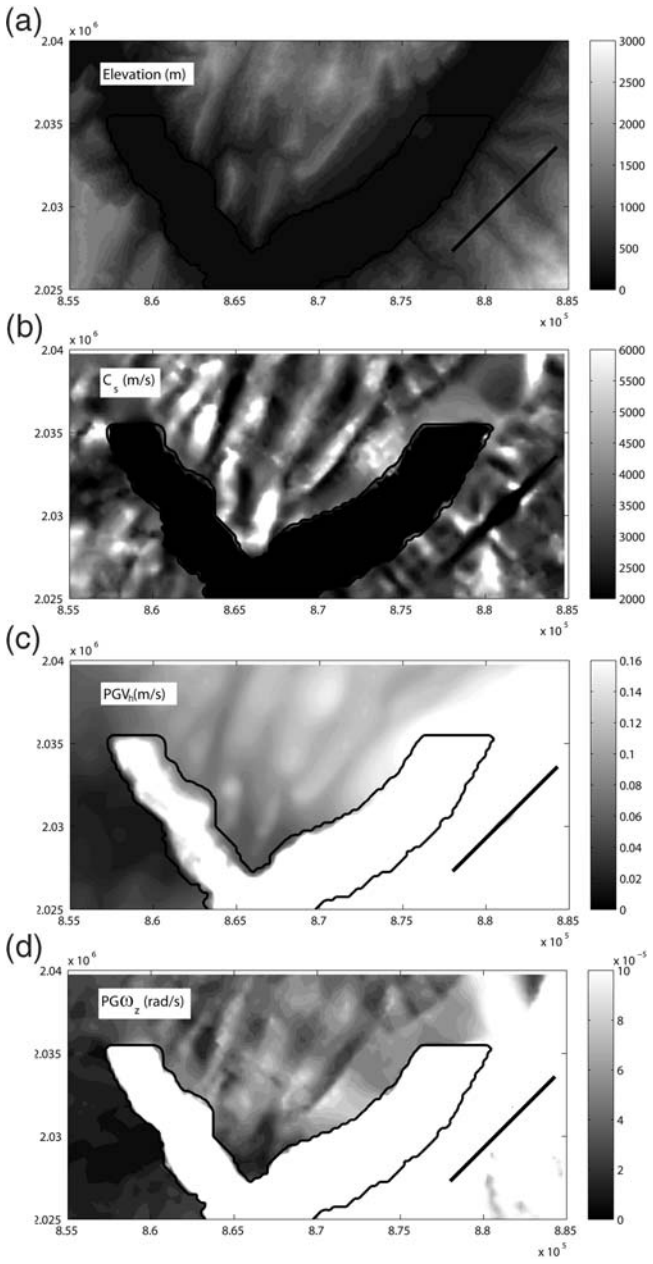

Figure 10. Effect of the topography on the peak motion values. (a) Map of the elevation of the northern part of the Grenoble area. (b) c_s values, which capture most of the topographic features seen in the elevation map. (c) PGV_h and (d) $PG\omega_z$ values, scaled in order to highlight variations in the zone of interest.

adequate scaling to observe variations in those peak values due to topography. The PGV_h map shows a clear topographic amplification as already investigated in other contexts by many authors (i.e., Géli *et al.*, 1988; Paolucci *et al.*, 1999). The vertical rotational motion seems to show a different and more complex pattern, related to the slope of the mountain and its convexity or concavity with respect to the direction from the radiation source.

Keeping in mind that the actual *S*-wave velocity has a value of 3200 m/sec, we can observe that strong variations occur at both sides of the mountains' crests due to the $PG\omega_z$ variations just discussed. All main topographic features in the region between both alluvial valleys are clearly visible in the c_s map. Finally, we can observe the fault trace in the c_s map as a zone of very low values, primarily due to the high values (roughly between 30 and 80 mrad/sec) of $PG\omega_z$ recorded locally, just on top of the fault.

Comparison between Grenoble Synthetics and Data of Past Studies

Adopting equation (1), we study the relation between rotational and translational motion for a collection of data that must be discussed carefully due to their different origins and qualities. We can basically divide the data in three distinct subgroups. The first subgroup is peak rotational and translational values obtained in past studies, mainly those labeled 1–16 in Table 1, for which we do not possess the whole time histories. A second data subgroup is field recordings, array-derived, for which detailed information is available, those labeled 17–24 in Table 1. In particular, 17–20 are data obtained by Paolucci and Smerzini (2008) through an empirical procedure based on a suitable spatial interpolation technique of displacement recordings from dense arrays at Parkway Valley, New Zealand (points 16 and 17), and U.S. Geological Survey Parkfield Dense Seismograph Array (UPSAR), California (points 18 and 19). For the data values 17–20 we plot the average value (filled circle) and their minimum and maximum value (denoted by bars). The estimates recently derived by Spudich and Fletcher (2008) for the 2004 M_w 6.0 Parkfield event and three aftershocks (in order of decreasing magnitude, M_w 5.1, M_w 4.9, and M_w 4.7), labeled from 21 to 24 in Table 1, are also used. In this case, we applied the so-called seismogeodetic approach to the UPSAR recordings in order to derive tilts and torsions. Referring to Spudich and Fletcher (2008), we considered three subarray estimates for each event, filtered in the frequency band between 0.1 and 1.4 Hz (points from 21 to 24) for comparison purposes with the southeast synthetics with a maximum frequency of 2 Hz. The third and last data subgroup is the synthetics obtained for the numerical study of the Grenoble valley for M_w 6.0 and M_w 4.5 scenarios, subdivided into records obtained at the outcropping bedrock and inside the alluvial basin. All synthetics used are computed for the case of neutral directivity and viscoelastic soil behavior.

The complete dataset is presented in Figure 11. Although the comparison is not straightforward (as we are combining a wide range of magnitudes, epicentral distances, and sources of data), when attention focuses on the synthetic PGV_h–$PG\omega_z$ pairs some interesting features can be noted. Primarily, the synthetic data, subdivided into alluvial and bedrock conditions, suggest a linear trend between PGV_h and $PG\omega_z$ in log–log space. In order to have a quantitative estimate of such a tendency, we decided to perform a linear regression of the synthetic data. The best-fitted lines turn out to be

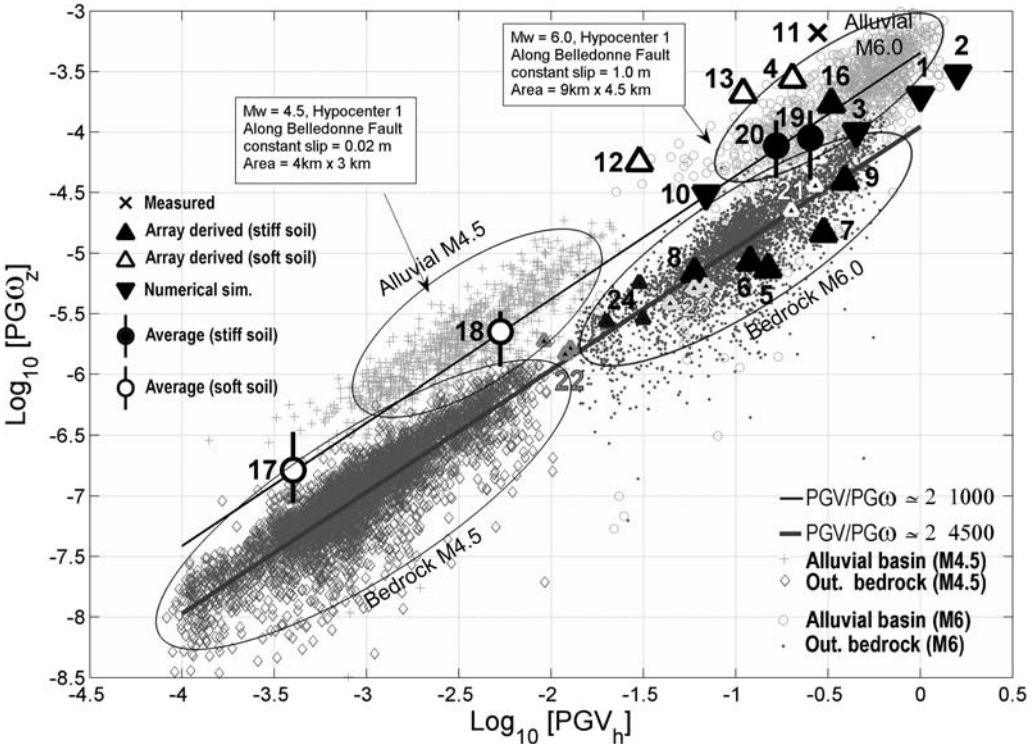

Figure 11. Synthetic values of peak ground horizontal velocity (PGV_h) versus peak ground rotation ($PG\omega_z$) in logarithmic scale obtained with M_w 6.0 and M_w 4.5, neutral directivity, and EL soil behavior. Superimposed are the individual data retrieved from literature, listed in Table 1. Data from 18 to 21 are plotted in terms of average value (filled circle) and their minimum and maximum value (denoted by bars).

$$\log_{10} PG\omega_z = \log_{10} PGV_h - 3.96 \tag{8}$$

at outcropping bedrock and

$$\log_{10} PG\omega_z = \log_{10} PGV_h - 3.34 \tag{9}$$

in the alluvial basin.

The coefficient of proportionality of both equations (8) and (9) is naturally very close to 1, suggesting a linear relationship between PGV_h and $PG\omega_z$ in agreement with equation (1), at least for the considered range of frequencies (0.1–2.0 Hz). Specifically, two straight lines superimposed in Figure 11 with $c_s \sim 4500$ m/sec (thick line) and $c_s \sim 1000$ m/sec (thin line) describe with reasonable accuracy the $PG\omega_z$ values obtained at the outcropping bedrock and on the basin, respectively, for both the M_w 4.5 and M_w 6.0 earthquake scenarios. If on one side synthetic data show a linear trend regardless of magnitude, the dependence on site effects turns out to be pronounced. Passing from soft alluvial conditions to outcropping bedrock, the $PGV_h/PG\omega_z$ ratio increases on average by about a factor of 4.

Nevertheless, it should be noted that the interpretation of c_s as the actual representative phase velocity V_a might be misleading. As also commented by Spudich and Fletcher (2008), c_s can be reasonably regarded as a scaling factor between peak rotations and translations rather than a true phase velocity at the selected model.

The array-derived estimates retrieved by Paolucci and Smerzini (2008) (points from 17 to 20) show very similar values and trend with respect to the synthetics. Their behavior alone is also remarkably linear, leading to $c_s \sim$ 1000 m/sec irrespective of the different site conditions. As a matter of fact, while points 17 and 18 fit fairly well with the synthetics calculated in the soft alluvial basin, points 19 and 20, which correspond more to bedrock conditions, seem to not be consistent with the ratio $c_s \sim 4500$ m/sec as inferred from the numerical simulations. The subarray estimates of Spudich and Fletcher (2008) (see points from 21 to 24) are consistent with synthetics provided the relatively stiff conditions of the UPSAR.

The single available direct measurement of the ratio $PGV_h/PG\omega_z$ seems to be significantly larger than all the simulated and array-derived estimates (point 13). However, this data refers to an explosion rather than an earthquake, so the comparison may be improper. Unfortunately, the measurements from Takeo (1998) cannot be used on the present study because only rotation rate records of the M_w 5.0 Ito, Japan, events are available. Nevertheless, Spudich and Fletcher (2008) also commented a substantial disagreement between Takeo's measurements and empirical estimates for the reasons briefly illustrated previously. Thus, his direct measurements of rotation rates turn out to be larger than other estimates by a factor of 5–60, and the ratio of $PGV_h/PG\omega_z$ is systemically higher than those of

the Parkfield and Chi-Chi earthquakes (see Spudich and Fletcher, 2008).

At this point, we can try to answer whether or not we can infer PGω_z from PGV$_h$. As a first approximation, it is clear that an average trend exists, mainly following equation (1), which allows for a rough estimation of the average rotational peak values given a suitable measure of the phase velocity at the receiver site. This might be helpful for quick estimates, although Figure 11 shows us the large variability displayed in the Grenoble area. This indicates that average values only are not sufficient to explain the complex behavior of rotational ground motions at the surface. More detailed pictures of rotational energy distribution should be obtained, preferably by deploying rotational sensors or seismometer arrays, in order to further identify more complex factors not only related to the local phase velocity but to other factors such as topography, spatial incoherence, or source-related effects.

Conclusions

In this article, we show a selection of available data concerning observed and synthetic rotational motion mainly regarding near-field and strong-motion earthquakes. The lack of observation testifies to the need to investigate more carefully the role of rotations, almost neglected in seismological and hazard assessment studies. Using two well-established and accurately validated numerical techniques (SEM and ADER-DG), we simulated the rotational wave field induced by an M_w 6.0 and an M_w 4.5 earthquake occurring in the valley of Grenoble (French Alps). The expected peak ground rotation (PGω) values on receivers located on soft soil is roughly 1 mrad, and the peak ground rotation rate (PG$\dot{\omega}$) is 10 mrad/sec. Those values show a strong dependence on the hypocenter location, the local site conditions, and the topographical features, inducing a variability of almost one order of magnitude in a range of distances of 20 km.

Numerical simulations also show a general trend correlating the maximum of rotational and translational motion. As a first approximation, the estimate of PGω_z can be regarded as linearly proportional to PGV$_h$, being the proportionality related to the mechanical properties of the medium around the receivers. Furthermore, this observation seems to be relatively independent of the magnitude of the earthquake. However, the overall collection of PGV$_h$–PGω_z pairs shows a large variability of up to two orders of magnitude around the average trend.

In conclusion, we remark on the need for records of rotational components of the seismic wave field coupled with classical translational motions, which can be achieved only with rotational sensors specifically designed. Only these kinds of records could assess a definitive answer to the relationship between velocity and rotation in the future and offer a set of data capable of explaining the large variability, which rotations seem to show.

Data and Resources

Detailed specification of the effects of surface geology on seismic motion (ESG) 2006 benchmark for ground-motion simulation in the Grenoble valley was provided by the organization committee to the benchmark participants. All other data used in this article came from published sources listed in the references. A more detailed description of information discussed in the Numerical Method Validation section can be found at http://geoelse.stru.polimi.it, last accessed February 2009.

Acknowledgments

This work benefited from the cooperation of many individuals and institutions during its different stages. This work was been financially supported by the Marie-Curie Training Network SPICE (Seismic Wave Propagation and Imaging in Complex Media). We deeply thank the Center for Advanced Studies, Research, and Development in Sardinia (CRS4) and, in particular, F. Maggio and L. Massidda for the essential cooperation in the development of the software GeoELSE; P. Spudich and J. Fletcher for providing the peak ground rotation and velocity values observed at the UPSAR array in Parkfield, California, and for fruitful discussion; R. Paolucci for useful suggestions; L. Scandella for collaborating to develop the subroutines for nonlinear elastic soil behavior; E. Chaljub for organizing the Grenoble benchmark and providing the necessary information for constructing and processing the numerical model; and E. Faccioli for his continuing support since the early stage of development of GeoELSE. We also gratefully acknowledge cooperation with the Leibniz Rechenzentrum in München, the Barcelona Supercomputing Center, and the HPC-Europa Transnational Access Program and the support of J. Oeser from the Department of Earth Sciences, Geophysics, in running the TETHYS cluster. We are also grateful to M. D. Trifunac, W. Lee, and an anonymous reviewer; their detailed revision helped us significantly in improving the manuscript.

References

Bodin, P., J. Gomberg, S. K. Singh, and M. Santoyo (1997). Dynamic deformations of shallow sediments in the Valley of Mexico, part I: Three-dimensional strains and rotations recorded on a seismic array, *Bull. Seismol. Soc. Am.* **87,** 528–539.

Bouchon, M., and K. Aki (1982). Strain, tilt, and rotation associated with strong ground motion in the vicinity of earthquake faults, *Bull. Seismol. Soc. Am.* **72,** 1717–1738.

Castellani, A., and G. Boffi (1986). Rotational components of the surface ground motion during an earthquake, *Earthq. Eng. Struct. Dyn.* **14,** no. 5, 751–767.

Chaljub, E. (2006). Numerical benchmark of 3D ground motion simulation in the valley of Grenoble, French Alps, http://esg2006.obs.ujf-grenoble.fr/BENCH2/benchmark.html (last accessed March 2009).

Chaljub, E., D. Komatitsch, J.-P. Vilotte, Y. Capdeville, B. Valette, and G. Festa (2007). Spectral element analysis in seismology, in *Advances in Wave Propagation in Heterogeneous Media*, Advances in Geophysics, R.-S. Wu and V. Maupin (Editors), Vol. **48**, Elsevier, Amsterdam, 365–419.

Cochard, A., H. Igel, A. Flaws, B. Schuberth, J. Wassermann, and W. Suryanto (2006). Rotational motions in seismology: theory, observation, simulation, in *Earthquake Source Asymmetry, Structural Media and Rotation Effects*, R. Teisseyre, E. Majewski, and M. Takeo (Editors), Springer, Berlin, 391–411, doi 10.1007/3-540-31337-0_30.

Day, S. M., J. Bielak, D. Dreger, R. Graves, S. Larsen, K. B. Olsen, and A. Pitarka (2001). Tests of 3D Elastodynamic Codes: Final Report for Lifelines Project 1A02, Technical Report, Pacific Earthquake Engineering Research Center, University of California, Berkeley.

Day, S. M., R. Graves, J. Bielak, D. Dreger, S. Larsen, K. B. Olsen, A. Pitarka, and L. Ramirez-Guzman (2007). Model for basin effects on long-period response spectra in southern California, *Earthq. Spectra* **24,** no. 1, 257–277.

Dumbser, M., and M. Käser (2006). An arbitrary high order discontinuous Galerkin method for elastic waves on unstructured meshes II: The three-dimensional isotropic case, *Geophys. J. Int.* **167,** 319–336.

Dumbser, M., M. Käser, and F. T. Eleuterio (2007). An arbitrary high-order discontinuous Galerkin method for elastic waves on unstructured meshes—V. Local time stepping and *p*-adaptivity, *Geophys. J. Int.* **171,** 695–717, doi 10.1111/j.1365-246X.2007.03427.x.

Faccioli, E., F. Maggio, R. Paolucci, and A. Quarteroni (1997). 2D and 3D elastic wave propagation by a pseudo-spectral domain decomposition method, *J. Seism.* **1,** 237–251.

Fichtner, A., and H. Igel (2009). Sensitivity densities for rotational ground-motion measurements, *Bull. Seismol. Soc. Am.* **99,** no. 2B, 1302–1314.

Géli, L., P.-Y. Bard, and B. Jullien (1988). The effect of topography on earthquake ground motion: A review and new results, *Bull. Seismol. Soc. Am.* **78,** 42–63.

Ghayamghamian, M. R., and G. R. Nouri (2007). On the characteristics of ground motion rotational components using Chiba dense array data, *Earthq. Eng. Struct. Dyn.* **36,** 1407–1429, doi 10.1002/eqe.687.

Graizer, V. M. (1989). Bearing on the problem of inertial seismometry, *Izv. Acad. Sci. USSR Phys. Solid Earth* **25,** no. 1, 26–29.

Graizer, V. M. (2005). Effect of tilt on ground motion data processing, *Soil Dyn. Earthq. Eng.* **25,** no. 3, 197–204.

Graizer, V. M. (2006a). Equation of pendulum motion including rotations and its implications to the strong-ground motion, in *Earthquake Source Asymmetry, Structural Media, and Rotation Effects*, R. Teisseyre, E. Majewski, and M. Takeo (Editors), Springer, Berlin, 471–491, doi 10.1007/3-540-31337-0_30.

Graizer, V. M. (2006b). Tilts in strong ground motion, *Bull. Seismol. Soc. Am.* **96,** no. 6, 2090–2102.

Gupta, V. K., and M. D. Trifunac (1989). Investigation of building response to translational and rotational earthquake excitations, Report CE 89–02, University of Southern California, Los Angeles, California.

Huang, B.-S. (2003). Ground rotational motions of the 1999 Chi-Chi, Taiwan, earthquake as inferred from dense array observations, *Geophys. Res. Lett.* **30,** 1307, doi 10.1029/2002GL015157.

Igel, H., A. Cochard, J. Wassermann, A. Flaws, U. Schreiber, A. Velikoseltsev, and N. Pham Dinh (2007). Broad-band observations of earthquake-induced rotational ground motions, *Geophys. J. Int.* **168,** 182–196, doi 10.1111/j.1365-246X.2006.03146.x.

Igel, H., U. Schreiber, A. Flaws, B. Schuberth, A. Velikoseltsev, and A. Cochard (2005). Rotational motions induced by the *M* 8.1 Tokachi-oki earthquake, September 25, 2003, *Geophys. Res. Lett.* **32,** L08309, doi 10.1029/2004GL022336.

Jerram, J., P. Foray, S. Labanieh, and E. Flavigny (2006). Characterising the nonlinearities of lacustrine clays in the Grenoble basin, in *Proc. 3rd Int. Symp. on the Effects of Surface Geology on Seismic Motion (ESG)*, Grenoble, France.

Kalkan, E., and V. Graizer (2007).Coupled tilt and translational ground motion response spectra, *ASCE J. Struct. Eng.* **133,** no. 5, 609–619.

Käser, M., and M. Dumbser (2006). An arbitrary high-order discontinuous Galerkin method for elastic waves on unstructured meshes—I. The two-dimensional isotropic case with external source terms, *Geophys. J. Int.* **166,** 855–877.

Komatitsch, D., and J. P. Vilotte (1998). The spectral element method: an efficient tool to simulate the seismic response of 2D and 3D geological structures, *Bull. Seismol. Soc. Am.* **88,** 368–392.

Kramer, S. L. (1996). *Geotechnical Earthquake Engineering*, Prentice Hall, Upper Saddle River, New Jersey.

Langston, C. A., W. H. K. Lee, C. J. Lin, and C. C. Liu (2009). Seismic-wave strain, rotation, and gradiometry for the 4 March 2008 TAIGER explosions, *Bull. Seismol. Soc. Am.* **99,** no. 2B, 1287–1301.

Lee, V. W., and M. D. Trifunac (1985). Torsional accelerograms, *Soil Dyn. Earthq. Eng.* **4,** no. 3, 132–142.

Lee, V. W., and M. D. Trifunac (1987). Rocking strong earthquake accelerations, *Soil Dyn. Earthq. Eng.* **6,** 75–89.

Lin, C.-J., C.-C. Liu, and W. H. K. Lee (2009). Recording rotational and translational ground motions of two TAIGER explosions in northeastern Taiwan on 4 March 2008, *Bull. Seismol. Soc. Am.* **99,** no. 2B, 1237–1250.

McLeod, D. P., G. E. Stedman, T. H. Webb, and U. Schreiber (1998). Comparison of standard and ring laser rotational seismograms, *Bull. Seismol. Soc. Am.* **88,** 1495–1503.

Newmark, N. M. (1969). Torsion in symmetrical buildings, in *Proc. Fourth World Conference on Earthquake Engineering*, Santiago, Chile, Vol. 3, 19–32.

Niazi, M. (1986). Inferred displacements, velocities and rotations of a long rigid foundation located at El Centro differential array site during the 1979 Imperial Valley, California earthquake, *Earthq. Eng. Struct. Dyn.* **14,** no. 4, 531–542.

Nigbor, R. L. (1994). Six-degree of freedom ground motion measurement, *Bull. Seismol. Soc. Am.* **84,** no. 4, 1665–1669.

Oeser, J., H.-P. Bunge, and M. Mohr (2006). Cluster Design in the Earth Sciences: TETHYS, in *High Performance Computing and Communications—Second International Conference, HPCC 2006, Munich, Germany*, Lecture Notes in Computer Science, M. Gerndt and D. Kranzlmüller (Editors), Vol. **4208**, Springer, Berlin, 31–40, doi 10.1007/11847366_4.

Oliveira, C. S., and B. A. Bolt (1989). Rotational components of surface strong ground motion, *Earthq. Eng. Struct. Dyn.* **18,** 517–526.

Pancha, A., T. H. Webb, G. E. Stedman, D. P. McLeod, and K. U. Schreiber (2000). Ring laser detection of rotations from teleseismic waves, *Geophys. Res. Lett.* **27,** 3553–3556.

Paolucci, R., and C. Smerzini (2008). Earthquake-induced transient ground strains from dense seismic networks, *Earthq. Spectra* **24,** no. 2, 453–470.

Paolucci, P., E. Faccioli, and F. Maggio (1999). 3D response analysis of an instrumented hill at Matsuzaki, Japan, by a spectral method, *J. Seism.* **3,** 191–209.

Pillet, R., and J. Virieux (2007). The effects of seismic rotations on inertial sensors, *Geophys. J. Int.* **171,** 1314–1323, doi 10.1111/j.1365-246X.2007.03617.x.

Priolo, E., J. M. Carcione, and G. Seriani (1994). Numerical simulation of interface waves by high-order spectral modeling techniques, *Acoust. Soc. Am.* **95,** 681–693.

Richter, C. F. (1958). *Elementary Seismology*, W. H. Freeman, San Francisco, 129–132.

Singh, S. K., M. Santoyo, P. Bodin, and J. Gomberg (1997). Dynamic deformations of shallow sediments in the Valley of Mexico, part II: Single-station estimates, *Bull. Seismol. Soc. Am.* **87,** 540–550.

Spudich, P., and J. Fletcher (2008). Observation and prediction of dynamic ground strains, tilts, and torsions caused by the M_w 6.0 2004 Parkfield, California, earthquake and aftershocks, derived from UPSAR array observations, *Bull. Seismol. Soc. Am.* **98,** no. 4, 1898–1914.

Spudich, P., L. K. Steck, M. Hellweg, J. Fletcher, and L. M. Baker (1995). Transient stresses at Parkfield, California, produced by the *M* 7.4 Landers earthquake of June 28, 1992: observations from the UPSAR dense seismograph array, *J. Geophys. Res.* **100,** 675–690.

Stacey, R. (1988). Improved transparent boundary formulations for the elastic wave equation, *Bull. Seismol. Soc. Am.* **78,** 2089–2097.

Stedman, G. E., Z. Li, and H. R. Bilger (1995). Side band analysis and seismic detection in a large ring laser, *Appl. Optics* **34,** 7390–7396.

Stratta, J. L., and T. F. Griswold (1976). Rotation of footing due to surface waves, *Bull. Seismol. Soc. Am.* **66,** no. 1, 105–108.

Stupazzini, M. (2004). A spectral element approach for 3D dynamic soil-structure interaction problems, *Ph.D. Thesis*, Politecnico di Milano, Italy.

Stupazzini, M., R. Paolucci, and H. Igel (2009). Near-fault earthquake ground motion simulation in the Grenoble Valley by a high-performance spectral element code, *Bull. Seismol. Soc. Am.* **99,** 286–301.

Suryanto, W., H. Igel, J. Wassermann, A. Cochard, B. Schuberth, D. Vollmer, F. Scherbaum, U. Schreiber, and A. Velikoseltsev (2006). First comparison of array-derived rotational ground motions with direct ring laser measurements, *Bull. Seismol. Soc. Am.* **96,** 2059–2071, doi 10.1785/0120060004.

Takeo, M. (1998). Ground rotational motions recorded in the near-source region of earthquakes, *Geophys. Res. Lett.* **25,** 789–792.

Takeo, M., and H. M. Ito (1997). What can be learned from rotational motions excited by earthquakes, *Geophys. J. Int.* **129,** 319–329.

Trifunac, M. D. (1982). A note on rotational components of earthquake motions for incident body waves, *Soil Dyn. Earthq. Eng.* **1,** 11–19.

Trifunac, M. D. (2009a). 75th anniversary of strong motion observation—a historical review, *Soil Dyn. Earthq. Eng.* **29,** no. 4, 591–606.

Trifunac, M. D. (2009b). Review: rotations in structural response, *Bull. Seismol. Soc. Am.* **99,** no. 2B, 968–979.

Trifunac, M. D., and M. I. Todorovska (2001). A note on the usable dynamic range of accelerographs recording translation, *Soil Dyn. Earthq. Eng.* **21,** no. 4, 275–286.

Wang, H., H. Igel, F. Gallovič, and A. Cochard (2009). Source and basin effects on rotational ground motions: comparison with translations, *Bull. Seismol. Soc. Am.* **99,** no. 2B, 1162–1173.

Department of Structural Engineering
Politecnico di Milano
P.zza Leonardo da Vinci 32
20133 Milano, Italy
stupa@stru.polimi.it
(M.S., A.C.)

Barcelona Center for Subsurface Imaging
Institut de Ciències del Mar, CSIC
Passeig Marítim de la Barceloneta, 37-49
08003 Barcelona, Spain
(J.D.)

Doctoral School of Earthquake Engineering and Engineering Seismology
ROSE School
via Ferrata 1
Pavia 27100, Italy
(C.S.)

Department für Geo- und Umweltwissenschaften Sektion Geophysik
Ludwig-Maximilians Universität
Theresienstrasse 41
80333 München, Germany
(M.K., H.I.)

Manuscript received 25 June 2008